Coherence and Decay of Higher Energy Levels of a Superconducting Transmon Qubit

Michael J. Peterer,[1,2,*] Samuel J. Bader,[1] Xiaoyue Jin,[1] Fei Yan,[1] Archana Kamal,[1] Theodore J. Gudmundsen,[3]
Peter J. Leek,[2] Terry P. Orlando,[1] William D. Oliver,[1,3] and Simon Gustavsson[1]
[1]*Research Laboratory of Electronics, Massachusetts Institute of Technology, Cambridge, Massachusetts 02139, USA*
[2]*Clarendon Laboratory, Department of Physics, University of Oxford, OX1 3PU Oxford, United Kingdom*
[3]*MIT Lincoln Laboratory, 244 Wood Street, Lexington, Massachusetts 02420, USA*

(Received 11 September 2014; revised manuscript received 11 November 2014; published 6 January 2015)

We present measurements of coherence and successive decay dynamics of higher energy levels of a superconducting transmon qubit. By applying consecutive π pulses for each sequential transition frequency, we excite the qubit from the ground state up to its fourth excited level and characterize the decay and coherence of each state. We find the decay to proceed mainly sequentially, with relaxation times in excess of 20 μs for all transitions. We also provide a direct measurement of the charge dispersion of these levels by analyzing beating patterns in Ramsey fringes. The results demonstrate the feasibility of using higher levels in transmon qubits for encoding quantum information.

DOI: 10.1103/PhysRevLett.114.010501 PACS numbers: 03.67.Lx, 05.40.Ca, 85.25.Cp

Universal quantum information processing is typically formulated with two-level quantum systems, or qubits [1]. However, extending the dimension of the Hilbert space to a d-level system, or "qudit," can provide significant computational advantages. In particular, qudits have been shown to reduce resource requirements [2,3], improve the efficiency of certain quantum cryptanalytic protocols [4–7], simplify the implementation of quantum gates [8,9], and have been used for simulating multidimensional quantum-mechanical systems [10]. The superconducting transmon qubit [11] is a quantum LC oscillator with the inductor replaced by a Josephson junction [Fig. 1(a)]. The nonlinearity of the Josephson inductance renders the oscillator weakly anharmonic, which allows selective addressing of the individual energy transitions and, thus, makes the device well-suited for investigating multilevel quantum systems. The transmon's energy potential is shallower than the parabolic potential of an harmonic oscillator, leading to energy levels that become more closely spaced as energy increases [Fig. 1(b)]. Although leakage to these levels can be a complication when operating the device as a two-level system [12], the existence of higher levels has proven useful for implementing certain quantum gates [13,14]. Full quantum state tomography of a transmon operated as a three-level qutrit has also been demonstrated [15].

In this Letter, we investigate the energy decay and the phase coherence of the first five energy levels of a transmon qubit embedded in a three-dimensional cavity [16]. We find the energy decay of the excited states to be predominantly sequential, with nonsequential decay rates suppressed by 2 orders of magnitude. The suppression is a direct consequence of the parity of the wave functions in analogy with the orbital selection rules governing transitions in natural atoms. We find that the sequential decay rates scale as i, where $i = 1, \ldots, 4$ is the initial excited state, thus, confirming the radiation scaling expected for harmonic oscillators [17,18]. The decay times remain in excess of 20 μs for all states up to $i = 4$, making them promising resources for quantum information processing applications. In addition, we characterize the quantum phase coherence of the higher levels by performing Ramsey-type interference experiments on each of the allowed transitions, and find strong beating in the resulting interference pattern, due to quasiparticle tunneling. This experimental result provides a direct measurement of the charge dispersion of the different levels [19–24].

Our device is a transmon qubit with a transition frequency $f_{01} = 4.97$ GHz for the first excited state, embedded in an aluminum 3D cavity with a bare fundamental mode $f_c = 11$ GHz, and thermally anchored at a base temperature of 15 mK inside a dilution refrigerator. The interactions between the qubit in state $|i\rangle$ and the cavity causes a dispersive shift χ_i of the cavity resonance to a new frequency $f_i = f_c + \chi_i$, which is exploited for the readout of the qubit state [25]. We probe the state by sending coherent readout microwaves of frequency $f_{\mu\mathrm{w}}$ through the resonator at a chosen detuning $\Delta_{\mu\mathrm{w}} = f_{\mu\mathrm{w}} - f_c$ from the bare cavity resonance, and measure the averaged transmission coefficient S_{21} of the signal over many experiments. Through a heterodyne detection scheme, the voltage amplitude of the transmission signal at $f_{\mu\mathrm{w}}$ is recorded, from which the qubit state occupation is then directly extracted. The resonator transmission takes the form of a Lorentzian peak $S_{21}^i(f_{\mu\mathrm{w}}) = p_i/[1 + 2\mathbf{i}Q_t(f_{\mu\mathrm{w}} - f_i)/f_i]$ (see [26]), centered around the qubit state-dependent frequency f_i, with magnitude p_i representing the state population, and Q_t the total quality factor. When the total population p is distributed over several states $|i\rangle$, the transmission becomes $S_{21}(f_{\mu\mathrm{w}}) = \sum_i S_{21}^i(f_{\mu\mathrm{w}})$.

Exciting the transmon to a higher level first requires us to measure and analyze Rabi oscillations between adjacent

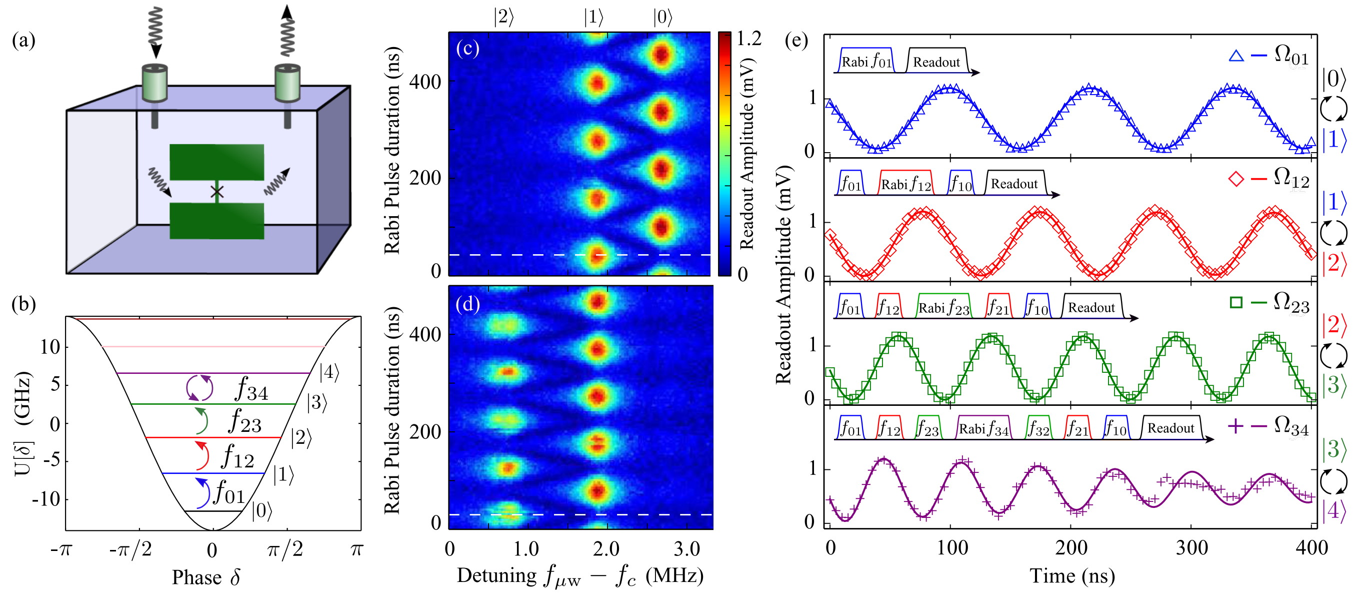

FIG. 1 (color online). (a) Schematic of the physical transmon qubit (not to scale) housed in the 3D cavity. The cross represents the Josephson junction, situated between the two junction electrodes forming the capacitor. (b) Simulated energy spectrum of the transmon with parameters $E_J/E_C = 58$, where $U[\delta]$ is the Josephson potential. (c) Rabi oscillations between state $|0\rangle$ and $|1\rangle$ under a Rabi drive tone of varying duration at f_{01}. The white dashed line indicates the position of the first π pulse at $\pi_{01} = 40$ ns. (d) Rabi oscillations between $|1\rangle$ and $|2\rangle$ with $\pi_{12} = 29$ ns, obtained by adding a Rabi drive tone at f_{12} after initializing state $|1\rangle$ by applying a π_{01} pulse. (e) Rabi oscillations on each successive qubit transition up to state $|4\rangle$ using the depopulation readout method. The corresponding excitation pulse sequence and respective depopulation sequence are shown for each Rabi drive. The solid lines are best-fit curves allowing the extraction of the Rabi frequencies Ω_{ij} as $\Omega_{01} = 8.45$ MHz, $\Omega_{12} = 10.3$ MHz, $\Omega_{23} = 13.0$ MHz, and $\Omega_{34} = 15.6$ MHz, respectively.

pairs of energy levels, working sequentially up the ladder of states, as depicted in Fig. 1(b). Combined with qubit spectroscopy at each step, this protocol allows us to obtain the successive transition frequencies up to $f_{i-1,i}$ and to accurately calibrate the corresponding π pulses. Starting with the qubit in the ground state $|0\rangle$, we apply a microwave pulse at f_{01} which drives the population between states $|0\rangle \leftrightarrow |1\rangle$ [see Fig. 1(c)]. As the qubit undergoes Rabi oscillations, the resonator transmission peak continuously rises and falls, oscillating between the discrete shifted resonance frequencies f_0 and f_1. Fitting the Rabi oscillations on state $|1\rangle$ permits us to experimentally extract the π pulse duration $\pi_{01} = 40$ ns from the white dashed line in Fig. 1(c), required to achieve a complete population transfer at transition frequency f_{01}. In the second step, we add a second Rabi drive tone at f_{12} promptly after the π_{01} pulse (with a delay of 70 ns, much shorter than the decay time Γ_{10}^{-1} from state 1 to 0), so as to perform Rabi oscillations between states $|1\rangle \leftrightarrow |2\rangle$, enabling the calibration of the second π pulse of duration $\pi_{12} = 29$ ns to reach $|2\rangle$. This process is repeated by adding a drive tone at each subsequent transition in order to calibrate the π pulses up to the desired state. These procedures also allow us to experimentally extract the dispersive shifts χ_i. A full numerical simulation of our coupled qubit-cavity Hamiltonian predicts all the qubit transition frequencies $f_{i-1,i}$ and the dispersive shifts χ_i, and they are in very good agreement with the experimentally obtained values, displayed in Table I.

When driving Rabi oscillations on the transition $|i\rangle \leftrightarrow |i+1\rangle$ for $i \geq 2$, the readout by the method presented above is not possible in this device, because state $|3\rangle$ does not appear as a conditional shift to the resonator. This is a consequence of the fact that certain states escape the dispersive regime due to their mixing with higher-excited states that have transition frequencies close to the resonator frequency, see simulation in [26]. As a result, we use a modified readout protocol, which does not require measurement pulses at the shifted resonance f_3 or f_4. After preparing the qubit in state $|i\rangle$ via the upward sequence of π pulses $S_i^{\uparrow} = (\pi_{01}, \pi_{12}, \ldots, \pi_{i-1,i})$, we additionally apply a depopulation sequence $S_i^{\downarrow} = (\pi_{i,i-1}, \ldots, \pi_{21}, \pi_{10})$ to the qubit immediately before the readout. This maps the population p_i of state $|i\rangle$ onto that of the ground state $|0\rangle$, allowing us to measure p_i by simply probing the resonator at the frequency f_0.

By incorporating the depopulation sequence, we are able to drive Rabi oscillations of the transmon up to state $|4\rangle$, as shown in Fig. 1(e). The Rabi frequencies Ω_{ij}, extracted via a best-fit curve, are proportional to the matrix elements $\langle i|\hat{n}|j\rangle$ between the states i and j, where $\hat{n}$ denotes the number of Cooper pairs transferred between the two

TABLE I. Comparison of experimental and simulated values for the transition frequencies $f_{i,i+1}$, the relaxation times Γ_{ij}^{-1} for the sequential and nonsequential decay rates, the dephasing times $T_{2(ij)}$ for the superpositions of states $|i\rangle$ and $|j\rangle$, and the dispersive shifts χ_i. The measured charge dispersion splittings $\epsilon_{ij}(n_g)$ extracted from Ramsey fringes are compared to the simulated maximum splittings $\epsilon_{ij}^{(\max)}$. The asterisks indicate the values that were fitted to the experiment for use as parameters in the full numerical simulation of the coupled qubit-cavity Hamiltonian.

Frequency	f_{01}^*	f_{12}^*	f_{23}	f_{34}
Experimental f (GHz)	4.9692	4.6944	4.3855	4.0280
Simulated f (GHz)	4.9692*	4.6944*	4.3874	4.0475
Sequential rate	Γ_{10}	Γ_{21}	Γ_{32}	Γ_{43}
and time (μs)	84 ± 0.24	41 ± 0.21	30 ± 0.21	22 ± 2
Nonsequential rate	Γ_{20}	Γ_{31}	Γ_{30}	
and time (ms)	1.8 ± 0.2	1.3 ± 0.4	2.6 ± 0.7	
Dephasing T_2	$T_{2(01)}$	$T_{2(12)}$	$T_{2(23)}$	$T_{2(34)}$
time (μs) $\pm 20\%$	72	32	12	<2

Qubit State i	$\|0\rangle$	$\|1\rangle$	$\|2\rangle$	$\|3\rangle$	$\|4\rangle$
Experimental χ_i (MHz)	2.8	2	0.88		
Simulated χ_i (MHz)	2.8*	2	0.85		
Experimental ϵ_{ij} (MHz)		$\cdots$	0.09	2.53	5–10
Simulated $\epsilon_{ij}^{(\max)}$ (MHz)		0.0025	0.091	1.89	26.8

junction electrodes forming the capacitor [26]. Consequently, Ω_{ij} increase as $\langle i|\hat{n}|j\rangle \propto \sqrt{j}$, as expected from the coupling between the transmon states and the resonator [11]. Thus, having obtained all the transition frequencies and π pulse calibrations, the qubit can be initialized in any state up to $|4\rangle$ with the sequence $S_4^{\uparrow}$, and we proceed to investigate the decay and phase coherence of these higher levels.

We start by measuring the dynamics of the state population decay by introducing a varying time delay before the readout process. The calibrated and normalized population evolutions starting from states $|1\rangle$, $|2\rangle$, and $|3\rangle$ are plotted in Figs. 2(a)–2(c). The decay from state $|4\rangle$ has also been measured and is presented in [26]. We model the data with a multilevel rate equation describing the evolution of the state population vector $\vec{p}$, with Γ_{ij} representing the decay rate from state i to state j: $\mathrm{d}\vec{p}(t)/\mathrm{d}t = \Gamma^{\mathrm{T}} \cdot \vec{p}(t)$. The decay rates matrix Γ has diagonal elements $(\Gamma)_{jj} = -\sum_{k=0}^{j-1} \Gamma_{jk}$ and off-diagonal elements Γ_{ij} for $i \neq j$. The upward rates are considered to be negligible by setting $\Gamma_{ij} = 0$ for all $i < j$, as $k_B T \ll h f_{ij}$ for all i, j. Indeed, the quiescent state-$|1\rangle$ population of our transmon is measured to be less than 0.1% [28]. The state occupations of the model are plotted (solid lines) and compared to the experimental data in Fig. 2 for each state, whereby the rates Γ_{ij} are used as fitting parameters to extract all the system's relaxation rates. The fitting was performed iteratively, starting with the decay from $|1\rangle$, where we fit Γ_{10} and then fix it for the next decay from $|2\rangle$, where Γ_{21} and Γ_{20} are determined, and so forth.

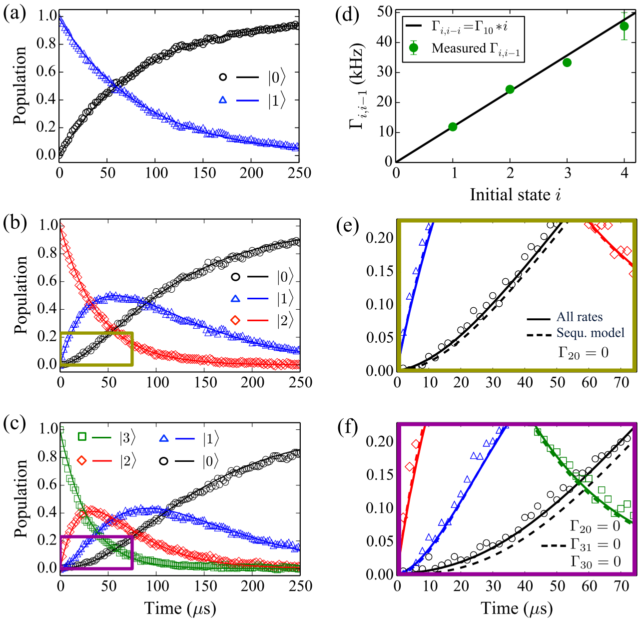

FIG. 2 (color online). (a)–(c) Population decay traces of the qubit states up to $|3\rangle$, obtained by varying the time delay Δt before the depopulation sequence. The solid lines are state occupations from the multilevel decay model taking into account all decay channels. (d) The sequential decay rates $\Gamma_{i,i-1}$ (green dots) for increasing energy state i, showing the roughly linear dependance (solid line). (e),(f) Zoom of decay curves in panels (b) and (c), respectively, showing the model with all transition rates allowed (solid line) compared to the model with only neighboring transitions allowed (dashed line). The extracted decay times are listed in Table I.

The most prominent feature of the data is that the decay proceeds mainly sequentially [29], with the nonsequential decay rates suppressed by 2 orders of magnitude. The extracted decay times are in excess of 20 μs for all states up to $|4\rangle$, and are listed in Table I. For the sequential rates, we find that the rates scale linearly with state i, as plotted in Fig. 2(d); this behavior is consistent with decay processes related to fluctuations of the electric field (like Purcell or dielectric losses), for which we expect the lifetimes to be inversely proportional to $|\langle i|\hat{n}|j\rangle|^2$ (see [26] for numerical calculations of the matrix elements). Furthermore, theoretical relaxation rates between neighboring levels due to quasiparticle tunneling also respect this approximate dependance $\Gamma_{i,i-1} \simeq i\Gamma_{10}$ [30,31]. We note that the anharmonicity of this device is sufficiently weak that its decay rates scale as those of Fock states in a harmonic oscillator [17,18].

To illustrate the effect of the nonsequential rates, we also fitted the data to a model involving only sequential rates [dashed lines in Figs. 2(e) and 2(f)]. Although the deviations between the two fits are small, inclusion of the rates

Γ_{20}^{-1}, Γ_{30}^{-1}, and Γ_{31}^{-1} does provide somewhat better matching for the initial increase in ground state population $|0\rangle$ for $t < 70\ \mu s$ where we would expect the largest impact. From numerical simulations of the qubit-resonator Hamiltonian, we expect the rates Γ_{20} and Γ_{31} to be strongly suppressed due to the parity of those states [32], whereas the matrix element $|\langle 3|\hat{n}|0\rangle|^2$ relevant for Γ_{30} is about 100 times smaller than $|\langle 1|\hat{n}|0\rangle|^2$ [26]. Quasiparticles also contribute to relaxation rates for non-neighboring levels, and theory [21] predicts that they are suppressed by at least 3 orders of magnitude, a much stronger suppression than we extract. This suggests that the nonsequential decay rates are dominated by some nonquasiparticle process, such as dielectric loss or coupling to other cavity modes.

We now proceed to investigate the phase coherence of the higher levels by performing a Ramsey-fringe measurement, whereby we obtain the dephasing times T_2. A Ramsey experiment on state $|i\rangle$ consists of first applying π pulses to bring the transmon to state $i-1$, followed by a $\pi/2$ pulse at frequency $f_{i-1,i}$ to bring it into a superposition of states $|i-1\rangle$ and $|i\rangle$, then allowing a variable free-evolution time Δt to pass, and finally applying a second $\pi/2$ pulse before applying the depopulation sequence and performing the readout. The measured Ramsey fringes are shown in Fig. 3 for each state up to $|4\rangle$. The frequency of the $\pi/2$ pulses was purposefully detuned to generate oscillating traces. The power spectral density of the data, obtained via a discrete Fourier transform, reveals two well-defined frequency components for states $|2\rangle$ and $|3\rangle$, and a number of frequencies for state $|4\rangle$. As described in the Supplemental Material [26], we fit the Ramsey fringes in Fig. 3(a) to a sum of two damped sinusoids, and the extracted dephasing times T_2 are listed in Table I.

The splitting of the transition frequencies can be understood in terms of quasiparticle tunneling between the two junction electrodes [26]. Despite the large E_J/E_C ratio, the transmon retains some sensitivity to charge fluctuations, and the charge dispersion approximately grows in an exponential way with increasing level number [26]. From our full numerical transmon-cavity simulation, we calculate the change in level splitting $\epsilon_{ij}(n_g)$ between levels i, j as a function of the effective offset charge n_g [11], shown in Fig. 4. The maximum change in ϵ_{ij} due to quasiparticle tunneling is given by $\epsilon_{ij}^{(\max)} = \epsilon_{ij}(n_g = 1/2) - \epsilon_{ij}(n_g = 0)$, as marked by vertical dashed lines, but note that what we measure experimentally is the dispersion between $n_g + 1/2$ and n_g for an unknown value of n_g. The measured splittings are compared to the calculated maximum splittings $\epsilon_{ij}^{(\max)}$ in Table I. State $|1\rangle$ is unresolved, in agreement with the small splitting of 2.5 kHz predicted, whereas we find that the splittings of states $|2\rangle$ and $|3\rangle$ are reasonably well predicted by the simulation. Charge traps between the substrate and the deposited metal film, or the presence of two-level fluctuators in the junction, also lead to charge fluctuations, possibly explaining the additional peaks seen in the spectrum of the state $|4\rangle$. It should be noted that, for quantum information purposes, the noise causing the beating in the Ramsey fringes can be refocused with an echo sequence by adding a temporally short π pulse (broad frequency spectrum) to the center of the Ramsey sequence [33].

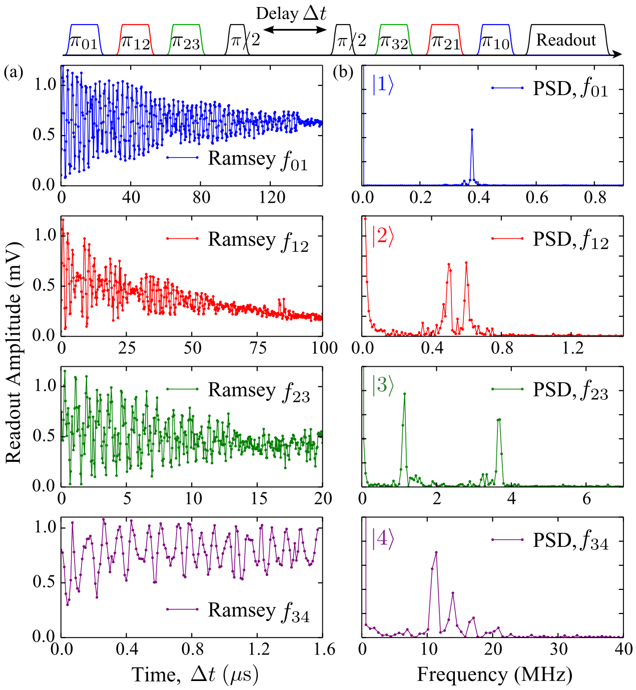

FIG. 3 (color online). (a) Ramsey oscillations experiment on each subsequent energy transition up to state $|4\rangle$. (b) The power spectral density (PSD), obtained from the discrete Fourier transforms of the corresponding Ramsey fringes. The Ramsey pulse sequence (top) corresponds to the fourth-row panel, representing a Ramsey sequence on state $|4\rangle$, with the black $\pi/2$ pulses representing the $\pi_{34}/2$ pulses performed at frequency f_{34} to bring the transmon into the superposition state $(|3\rangle + |4\rangle)/\sqrt{2}$ before allowing the free evolution time Δt.

In conclusion, we have demonstrated the preparation and control of the five lowest states of a transmon qubit in a

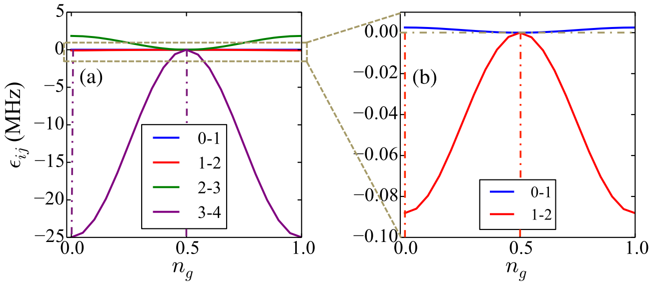

FIG. 4 (color online). (a) Calculated change in transition frequency $\epsilon_{ij}(n_g)$ as a function of the effective offset charge n_g, expressing the charge dispersion of each transition. (b) Zoom of the lowest two transitions 0-1 and 1-2.

three-dimensional cavity. We observed predominantly sequential energy relaxation, with nonsequential rates suppressed by 2 orders of magnitude. In addition, our direct measurement of the charge dispersion at higher levels agrees well with theory and facilitates further studies of the crucially important dephasing characteristics of quantum circuits. The measured qubit lifetimes in excess of 20 μs at energy states up to $|4\rangle$ expands the practicability of transmons for quantum information applications and simulations using multilevel systems.

We thank G. Catelani, J. Bylander, A. P. Sears, D. Hover, J. Yoder, and A. J. Kerman for helpful discussions, as well as Rick Slattery for assistance with the cavity design and fabrication, and George Fitch for assistance with layout. This research was funded in part by the Assistant Secretary of Defense for Research and Engineering under Air Force Contract No. FA8721-05-C-0002, by the U.S. Army Research Office (Contract No. W911NF-14-1-0078), and by the National Science Foundation (Grant No. PHY-1415514). M. J. P. and P. J. L. acknowledge funding from the UK Engineering and Physical Sciences Research Council.

---

[*] michael.peterer@physics.ox.ac.uk

[1] M. A. Nielson and I. L. Chuang, *Quantum Computation and Quantum Information* (Cambridge University Press, Cambridge, England, 2010).
[2] A. Muthukrishnan and C. R. Stroud, Phys. Rev. A **62**, 052309 (2000).
[3] S. S. Bullock, D. P. O'Leary, and G. K. Brennen, Phys. Rev. Lett. **94**, 230502 (2005).
[4] H. Bechmann-Pasquinucci and A. Peres, Phys. Rev. Lett. **85**, 3313 (2000).
[5] N. J. Cerf, M. Bourennane, A. Karlsson, and N. Gisin, Phys. Rev. Lett. **88**, 127902 (2002).
[6] T. Durt, D. Kaszlikowski, J.-L. Chen, and L. C. Kwek, Phys. Rev. A **69**, 032313 (2004).
[7] I. Bregman, D. Aharonov, M. Ben-Or, and H. S. Eisenberg, Phys. Rev. A **77**, 050301 (2008).
[8] B. P. Lanyon, M. Barbieri, M. P. Almeida, T. Jennewein, T. C. Ralph, K. J. Resch, G. J. Pryde, J. L. O'Brien, A. Gilchrist, and A. G. White, Nat. Phys. **5**, 134 (2009).
[9] J. M. Chow, J. M. Gambetta, A. W. Cross, S. T. Merkel, C. Rigetti, and M. Steffen, New J. Phys. **15**, 115012 (2013).
[10] M. Neeley, M. Ansmann, R. C. Bialczak, M. Hofheinz, E. Lucero, A. D. O'Connell, D. Sank, H. Wang, J. Wenner, A. N. Cleland, M. R. Geller, and J. M. Martinis, Science **325**, 722 (2009).
[11] J. Koch, T. M. Yu, J. Gambetta, A. A. Houck, D. I. Schuster, J. Majer, A. Blais, M. H. Devoret, S. M. Girvin, and R. J. Schoelkopf, Phys. Rev. A **76**, 042319 (2007).
[12] J. M. Chow, L. DiCarlo, J. M. Gambetta, F. Motzoi, L. Frunzio, S. M. Girvin, and R. J. Schoelkopf, Phys. Rev. A **82**, 040305 (2010).
[13] L. DiCarlo, J. M. Chow, J. M. Gambetta, L. S. Bishop, B. R. Johnson, D. I. Schuster, J. Majer, A. Blais, L. Frunzio, S. M. Girvin, and R. J. Schoelkopf, Nature (London) **460**, 240 (2009).
[14] A. A. Abdumalikov, J. M. Fink, K. Juliusson, M. Pechal, S. Berger, A. Wallraff, and S. Filipp, Nature (London) **496**, 482 (2013).
[15] R. Bianchetti, S. Filipp, M. Baur, J. M. Fink, C. Lang, L. Steffen, M. Boissonneault, A. Blais, and A. Wallraff, Phys. Rev. Lett. **105**, 223601 (2010).
[16] H. Paik, D. I. Schuster, L. S. Bishop, G. Kirchmair, G. Catelani, A. P. Sears, B. R. Johnson, M. J. Reagor, L. Frunzio, L. I. Glazman, S. M. Girvin, M. H. Devoret, and R. J. Schoelkopf, Phys. Rev. Lett. **107**, 240501 (2011).
[17] N. Lu, Phys. Rev. A **40**, 1707 (1989).
[18] H. Wang, M. Hofheinz, M. Ansmann, R. C. Bialczak, E. Lucero, M. Neeley, A. D. O'connell, D. Sank, J. Wenner, A. N. Cleland, and J. M. Martinis, Phys. Rev. Lett. **101**, 240401 (2008).
[19] J. A. Schreier, A. A. Houck, J. Koch, D. I. Schuster, B. R. Johnson, J. M. Chow, J. M. Gambetta, J. Majer, L. Frunzio, M. H. Devoret, S. M. Girvin, and R. J. Schoelkopf, Phys. Rev. B **77**, 180502 (2008).
[20] A. A. Houck, J. A. Schreier, B. R. Johnson, J. M. Chow, J. Koch, J. M. Gambetta, D. I. Schuster, L. Frunzio, M. H. Devoret, S. M. Girvin, and R. J. Schoelkopf, Phys. Rev. Lett. **101**, 080502 (2008).
[21] G. Catelani, S. E. Nigg, S. M. Girvin, R. J. Schoelkopf, and L. I. Glazman, Phys. Rev. B **86**, 184514 (2012).
[22] L. Sun, L. DiCarlo, M. D. Reed, G. Catelani, L. S. Bishop, D. I. Schuster, B. R. Johnson, G. A. Yang, L. Frunzio, L. Glazman, M. H. Devoret, and R. J. Schoelkopf, Phys. Rev. Lett. **108**, 230509 (2012).
[23] C. Wang, Y. Y. Gao, I. M. Pop, U. Vool, C. Axline, T. Brecht, R. W. Heeres, L. Frunzio, M. H. Devoret, G. Catelani, L. I. Glazman, and R. J. Schoelkopf, arXiv:1406.7300.
[24] D. Ristè, C. C. Bultink, M. J. Tiggelman, R. N. Schouten, K. W. Lehnert, and L. DiCarlo, Nat. Commun. **4**, 1913 (2013).
[25] A. Wallraff, D. I. Schuster, A. Blais, L. Frunzio, J. Majer, M. H. Devoret, S. M. Girvin, and R. J. Schoelkopf, Phys. Rev. Lett. **95**, 060501 (2005).
[26] See Supplemental Material at http://link.aps.org/supplemental/10.1103/PhysRevLett.114.010501, which includes Ref. [27], for further description of the measurement techniques, data analysis, further data to Fig. 2, and for the full numerical simulation of the transmon and the coupled qubit-cavity Hamiltonian.
[27] A. Blais, R.-S. Huang, A. Wallraff, S. M. Girvin, and R. J. Schoelkopf, Phys. Rev. A **69**, 062320 (2004).
[28] X. Y. Jin *et al.* (to be published).
[29] M. Dykman and M. Krivoglaz, Sov. Sci. Rev. **5**, 265 (1984).
[30] G. Catelani, J. Koch, L. Frunzio, R. J. Schoelkopf, M. H. Devoret, and L. I. Glazman, Phys. Rev. Lett. **106**, 077002 (2011).
[31] G. Catelani, R. J. Schoelkopf, M. H. Devoret, and L. I. Glazman, Phys. Rev. B **84**, 064517 (2011).
[32] F. Deppe, M. Mariantoni, E. Solano, and R. Gross, Nat. Phys. **4**, 686 (2008).
[33] E. L. Hahn, Phys. Rev. **80**, 580 (1950).